BEILSTEIN JOURNAL OF ORGANIC CHEMISTRY

A cyanine dimerization rendering positive cooperativity in molar absorptivity

Bingya Wang[1], Qin Yan[1], Bei Zhao[2], Guangbo Ge[2], Xuhong Qian[1,3], Xiao Luo[3] and Youjun Yang[*1]

Full Research Paper

Open Access

Address:
[1]State Key Laboratory of Bioreactor Engineering, Shanghai Key Laboratory of Chemical Biology, School of Pharmacy, East China University of Science and Technology, Meilong Road 130, Shanghai 200237, China, [2]State Key Laboratory of Discovery and Utilization of Functional Components in Traditional Chinese Medicine, Shanghai Frontiers Science Center of TCM Chemical Biology, Institute of Interdisciplinary Integrative Medicine Research, Shanghai University of Traditional Chinese Medicine, Shanghai 201203, China and [3]Shanghai Engineering Research Center of Molecular Therapeutics and New Drug Development, School of Chemistry and Molecular Engineering, East China Normal University, Dongchuan Road 500, Shanghai 200241, China

Email:
Youjun Yang[*] - youjunyang@ecust.edu.cn

* Corresponding author

Keywords:
cyanine dimers; molar absorptivity; positive cooperativity; single-bond tethering; vascular and lymphatic imaging

Beilstein J. Org. Chem. **2026,** *22,* 1803–1812.
https://doi.org/10.3762/bjoc.22.146

Received: 29 September 2026
Accepted: 13 November 2026
Published: 26 November 2026

This article is part of the thematic issue "Physical organic chemistry of new materials".

Guest Editor: J. D. Tovar



© 2026 Wang et al.; licensee Beilstein-Institut.
License and terms: see end of document.

Abstract

Enhancing the molar absorptivity of a dye or aggregate is an important and yet rarely pursued challenge. Herein, we report that single-bond-tethered cyanine dimers (**CyD7**, **CyD7.5**, **CyD7Et**, and **CyD7Bn**) among all different dimerization approaches render positive cooperativity in molar absorptivity. Namely, the molar absorptivity of the dimer in CH_2Cl_2 is higher than twice that of the monomer **M780**. Unusually high molar absorptivities of 648,000–701,000 $M^{-1}{\cdot}cm^{-1}$ are registered. The dimers were fluorescent and nano-encapsulated **CyD7Bn** was employed in high-contrast NIR fluorescence imaging of the systemic vasculature and long-term lymphatic imaging. These results suggest that single-bond-tethered dimerization is a useful strategy for preparing photofunctional materials with ultrahigh molar absorptivity.

Introduction

The most fundamental property of a dye beyond its absorption wavelength (λ_{abs}) is its molar absorptivity (ε). The higher the molar absorptivity, the lower the concentration required to achieve a target absorbance, endowing these dyes with broad application potential across diverse fields. In optoelectronic devices [1], high molar absorptivity facilitates thin-film device fabrication, suppresses charge recombination, and enhances external quantum efficiencies. In photodynamic/photothermal therapy [2], it ensures effective generation of reactive oxygen species or localized thermal ablation under low light intensity.

In bioimaging [3], it substantially improves dye brightness and tissue penetration depth, enabling high-contrast in vivo visualization. Nevertheless, the molar absorptivity of a dye or its aggregate has long been regarded as a "natural gift" rather than an engineerable parameter. Consequently, the rational design of molecular engineering systems with ultrahigh molar absorptivity has become a central objective in photofunctional materials research.

The key to enhancing molar absorptivity is to improve the transition dipole moment of a dye or dye aggregate. As for the monomeric dye, this may be achieved by quantum confinement (cyanine, ε = 501,000 $M^{-1}·cm^{-1}$) [4], multiple resonance effects [5], or D–π–A–π–D conjugated engineering [6]. In comparison, the structure–property relationships of dye aggregates have not been systematically explored. The degree of aggregation is a governing parameter of molar absorptivity. This work aims to provide initial insight into this topic, and we hence focus on the simplest of all aggregates, i.e., the dimer. The knowledge gained by studying dimers will serve as a stepping stone to more advanced dye aggregates. The proximal spatial arrangement of two or more chromophores induces exciton coupling, which further differently impacts the transition dipole moments. Consider the different dimers of cyanine dyes as examples. Fan and co-workers [7,8] reported a series of cyanine dimers by connecting two Cy5 dyes at the *N*-indole site with nonconjugated *ortho*/*meta*/*para*-bis(bromomethyl)benzene linkers, in which the molar absorptivity of the J-dimers is 1.3–1.8 times of the monomer (Figure 1a). Recently, Peng and co-workers [9,10] synthesized a special cyanine J-dimer by fusing their terminal benzene moiety. Its molar absorptivity was 1.6-fold of the monomer (Figure 1b). A series of H-aggregated cyanine dimers were reported [11-14] by linking two cyclohexene moieties with a single bond, displacing the *meso*-chloro atom of two cyanine dyes with a hydroquinone, or using the twisted conjugated motif tetraphenylethylene. The molar absorptivity of the H-dimers is typically 1.1–1.7 times of the corresponding monomer (Figure 1c). In 2025, we reported a V-dimer of cyanine dyes [14]. Its molar absorptivity was 1.3-fold of the monomer (Figure 1d). Thus, regardless of the dimerization approach, the molar absorption of the dimer is smaller than the sum of the molar absorptivity of the two monomers. Is it possible for the molar absorptivity of the dimer to exhibit positive cooperativity and be larger than the sum of the two monomers? We envisage that excitonic coupling is the strongest when the two dyes are held in close proximity with their transition dipole moments perfectly aligned. Peng et al. showcased that the two dyes are best not to share the terminal benzene moiety. Therefore, we proposed to link the two cyanine dyes into a perfectly aligned dimer using a single bond, and this design led to the single-bond-tethered cyanine dimers (**CyD7** and derivatives).

In this work, we report the design and synthesis of four single-bond-tethered cyanine dimers, **CyD7**, **CyD7.5**, **CyD7Et**, and **CyD7Bn**, along with the monomer **M780** as a reference. Their photophysical properties were acquired in different solvents. Regardless of the push–pull end groups, their molar absorptivity was more than twice that of the monomer, reaching 648,000–701,000 $M^{-1}·cm^{-1}$ in CH_2Cl_2. Davydov-splitted, red-shifted NIR absorption, and shortened fluorescence lifetimes further confirmed strong intramolecular exciton coupling. To highlight their potential for in vivo bioimaging, **CyD7Bn** in DSPE-mPEG2000 nanoparticles was showcased to be feasible for high-contrast whole-body vascular imaging and long-term lymphatic imaging in mice.

Results and Discussion

Synthesis of intermediates and dyes

The synthetic routes to the key intermediates and target dimers are depicted in Scheme 1 and Figure 2. All compounds were characterized by ^1H NMR, ^{13}C NMR, and HRMS (Figures S7–S36 in Supporting Information File 1). First, 4,4'-diaminobiphenyl (**1**) was converted to hydrazine **2** via diazotization ($NaNO_2$, HCl) and reduction (Se, $SnCl_2$). A classical Fischer indole synthesis with 3-methyl-2-butanone in acetic acid afforded bis-indole **3** (68%), which was alkylated with iodoethane to afford bis-indolium salt **M1** (53%). Second, indolium salt **M2** (94%) and benzindolium salt **M3** (87%) were prepared from 2,3,3-trimethyl-3*H*-indole (**4**) and 1,1,2-trimethyl-1*H*-benzo[*e*]indole (**5**), respectively. Compounds **6**–**9** and **N1** were synthesized according to literature procedures [4]. Hemicyanine dyes **W1**–**W4** (55–83%) were obtained by condensation reactions in toluene using acetic acid as the catalyst and **N1**. Finally, condensation–dehydration of intermediates **W1**–**W4** with bis-indolium salt **M1** afforded the target dimers **CyD7** (35%), **CyD7.5** (41%), **CyD7Et** (32%), and **CyD7Bn** (47%).

In vitro photophysical properties

The photophysical properties of monomer **M780** and dimers **CyD7**, **CyD7.5**, **CyD7Et**, and **CyD7Bn** in various organic solvents are shown in Figures S1–S5 in Supporting Information File 1, and the corresponding optical data are summarized in Table 1. The spectroscopic analysis in CH_2Cl_2 is presented as a representative case. In the UV–vis absorption spectra, monomer **M780** displayed an absorption maximum at 788 nm (ε = 283,000 $M^{-1}·cm^{-1}$), a weaker shoulder peak at 720 nm (ε = 48,000 $M^{-1}·cm^{-1}$), and negligible absorbance below 600 nm. This NIR window effectively circumvents the strong absorption of water and hemoglobin in biological tissues [15], favoring deep-tissue imaging in vivo. Compared with the monomer, the dimers **CyD7**, **CyD7.5**, **CyD7Et**, and **CyD7Bn** exhibited three split and broadened NIR absorption bands, consistent

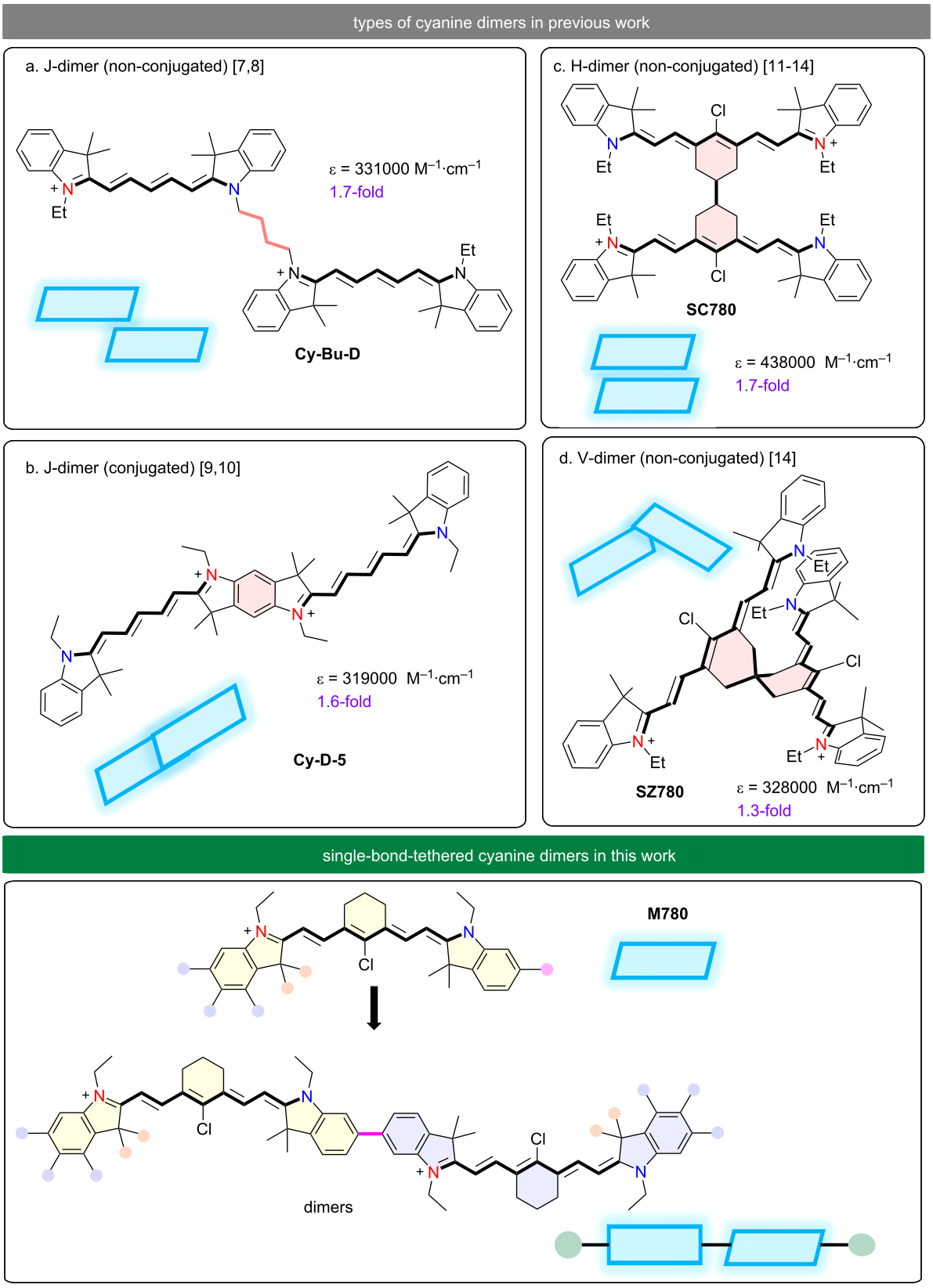

Figure 1: Rational design of the cyanine dimers **CyD7** and derivatives.

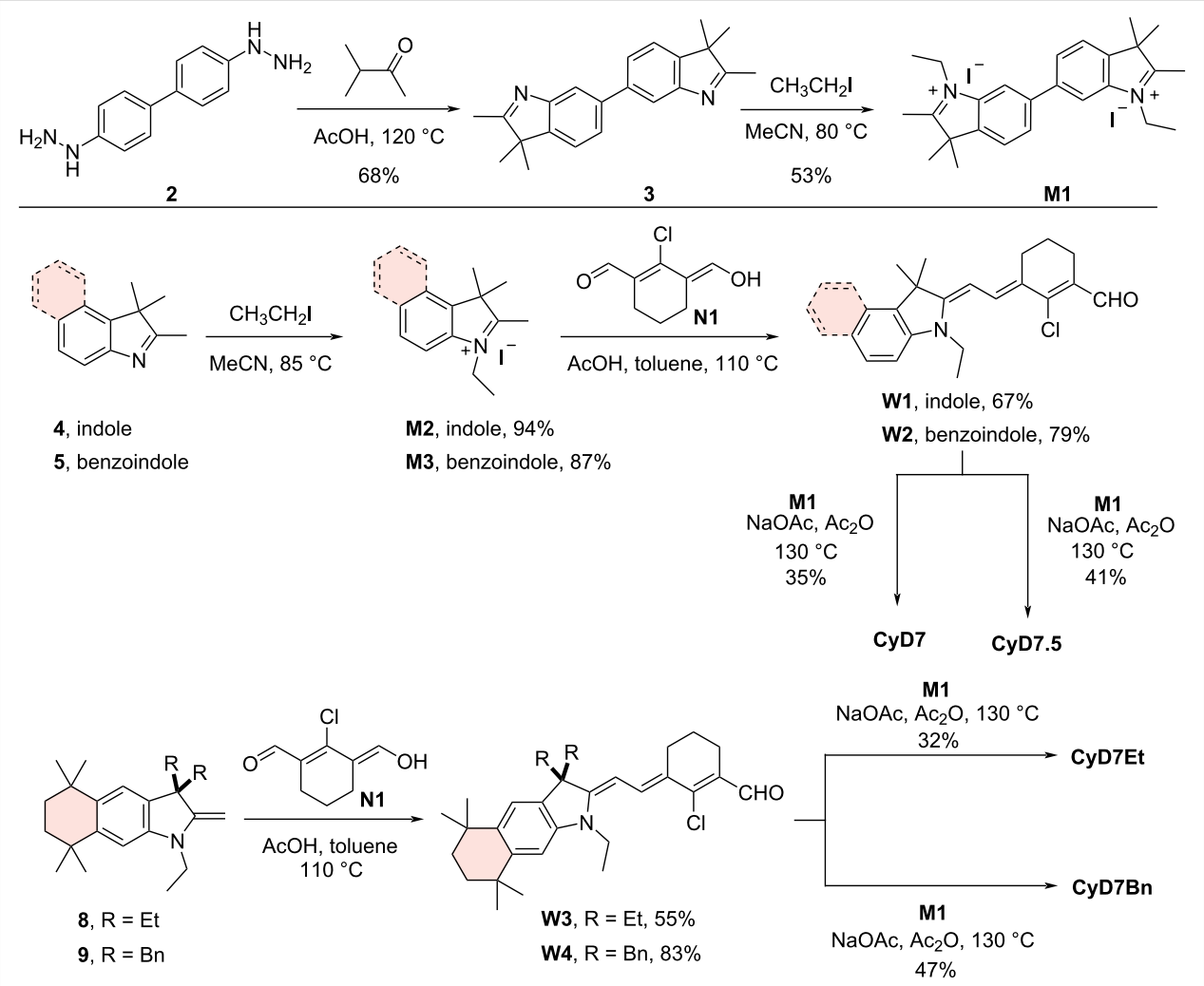

Scheme 1: Synthetic route of the cyanine dimers **CyD7** and derivatives.

with a Davydov splitting effect [16], their absorption maximum were observed at 857 nm (ε = 678,000 $M^{-1}·cm^{-1}$), 873 nm (648,000 $M^{-1}·cm^{-1}$), 861 nm (701,000 $M^{-1}·cm^{-1}$), and 877 nm (679,000 $M^{-1}·cm^{-1}$), respectively, with only a 69–88 nm red shift relative to the monomer. This suggested that the single-bond tether only mildly perturbs the internal electronic distribution of the dimers, thereby restricting π-electron delocalization between the two chromophores. Meanwhile, medium-intensity shoulders were appeared at 749 nm, 762 nm, 754 nm, and 764 nm (ε = 276,000–311,000 $M^{-1}·cm^{-1}$, Figure 3a). Notably, the molar absorptivities of the dimers were 2.3- to 2.5-fold of the monomer (Figure 3b). This unusual "1 + 1 > 2" absorption enhancement was attributed to a cooperative light-harvesting effect arising from intramolecular exciton coupling in the single-bond-tethered cyanine dimers. In the fluorescence emission spectra, monomer **M780** showed an emission maximum at 818 nm (Φ = 18.4%), with the emission spectrum ($S_1 \rightarrow S_0$) exhibiting a near mirror-image relationship to the absorption spectrum ($S_0 \rightarrow S_1$). In contrast, the dimers exhibited red-shifted emission maxima at 912 nm (Φ = 1.3%) for **CyD7**, 927 nm (Φ = 1.4%) for **CyD7.5**, 915 nm (Φ = 1.3%) for **CyD7Et**, and 931 nm (Φ = 1.7%) for **CyD7Bn**, along with substantially reduced fluorescence quantum yields (Figure 3c). As the fluorescence lifetime of a dye serves as a direct measure of excited-state relaxation dynamics [17], the effect of structural modification on the excited-state dynamic behavior was further investigated (Supporting Information File 1, Figure S6). A relatively long fluorescence lifetime (τ = 1.06 ns) was observed for monomer **M780**, whereas markedly shortened lifetimes of 0.17 ns, 0.24 ns, 0.19 ns, and 0.17 ns were observed for the dimers, respectively. The concurrent attenuation of these two key photophysical parameters indicated that the excited-state energy of the dimers was predominantly dissipated through non-radiative pathways, including intersystem crossing to the triplet excited state or internal conversion to heat. Finally, the overall fluorescence brightness

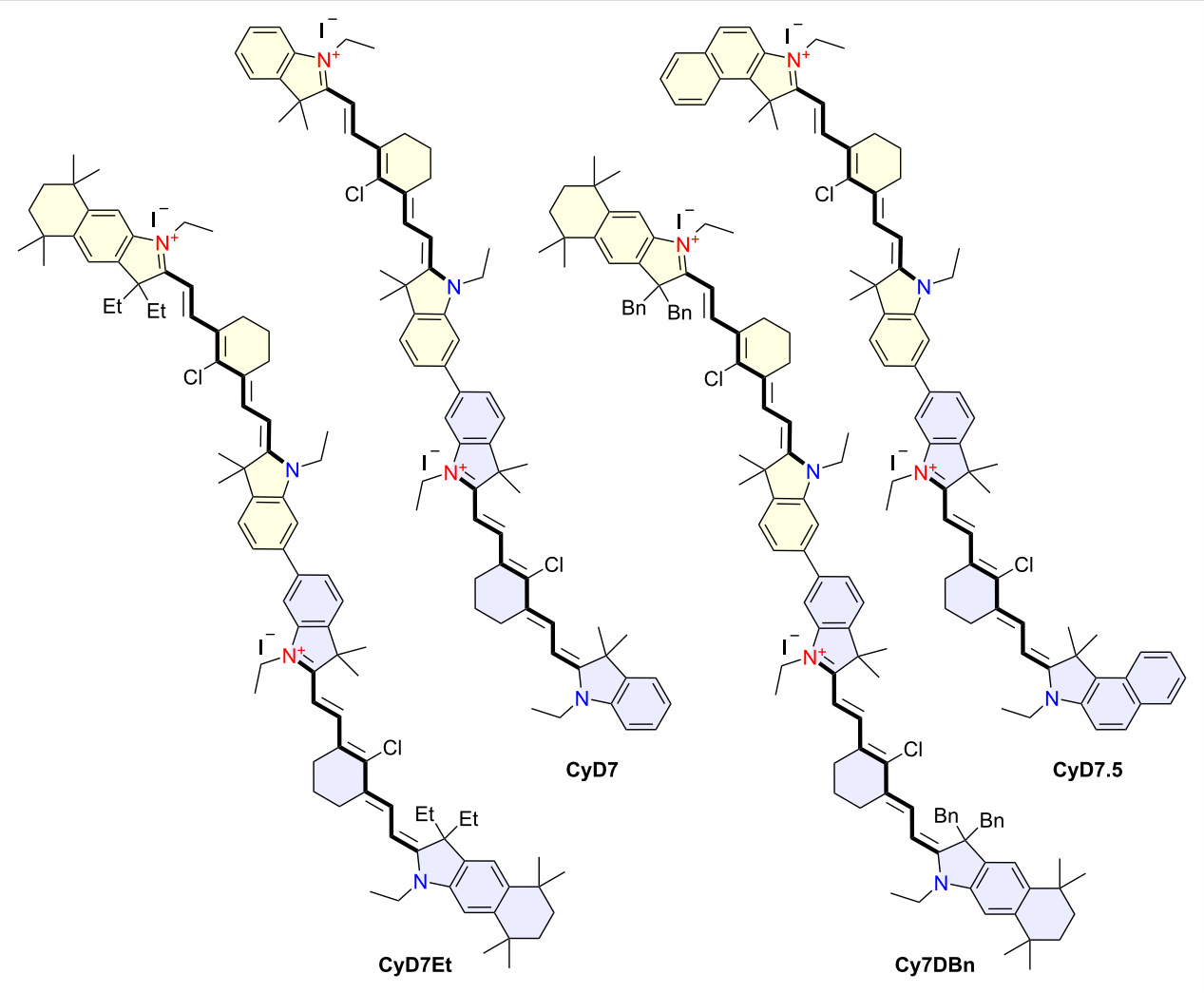

Figure 2: Structures of the cyanine dimers **CyD7** and derivatives.

($\varepsilon \times \Phi_F$) of dimer **CyD7Bn** remained above 10,000 $M^{-1}{\cdot}cm^{-1}$, considerably higher than those of most previously reported NIR dimeric dyes, indicating its potential for in vivo imaging applications.

In vivo NIR fluorescence imaging of whole-body vascular system

To prolong the blood circulation time and improve the biocompatibility of the hydrophobic dye, **CyD7Bn** NPs were prepared by encapsulating the dye with the amphiphilic block copolymer DSPE-mPEG2000. BALB/c mice (6–8 weeks old, body weight 20 ± 2 g) were intravenously injected with **CyD7Bn** NPs (100 µL, 1 mg/kg) via the tail vein. Whole-body vascular fluorescence images were acquired under 880 nm laser excitation using different long-pass filters (Figure 4a–e). With increasing cutoff wavelengths of the long-pass filters, the signal-to-background ratio (SBR) in the hindlimb vascular region (ROI-1) increased from 1.27 to 3.73, while the full width at half-maximum (FWHM) decreased from 0.71 mm to 0.49 mm. The signal-to-noise ratios (SNR) in the bladder region (ROI-2) were 1.76 and 1.56, respectively.

The precise discrimination between the femoral artery and femoral vein holds significant clinical value for the early diagnosis of peripheral vascular diseases and the assessment of hemodynamics [18,19]. To achieve high-resolution imaging of the hindlimb vasculature, the imaging mode was switched from wide-field to stereo microscopy, and the field of view was adjusted to 0.64× to clearly resolve the femoral vein and femoral artery (Figure 4f–h). Under the 1350 nm long-pass filter, Gaussian peak fitting yielded vessel diameters of 0.082 mm for the femoral vein and 0.132 mm for the femoral artery, with SBR exceeding 2.60. These results demonstrated that **CyD7Bn** NPs possessed submillimeter spatial resolution and were capable of accurately distinguishing adjacent microvessels.

Table 1: Photophysical parameters of monomer and dimers in different solvents.

dye	solvent	λ_{abs} (nm)	ε (M^{-1}·cm^{-1})	λ_{em} (nm)	Stokes shift (nm)	Φ_F[a] (%)	brightness[b] (M^{-1}·cm^{-1})	τ (ns)	k_r (10^9, s^{-1})	k_{nr} (10^9, s^{-1})
M780	CH_2Cl_2	788	283,000	818	30	18.4	52072	1.06	0.17	0.77
	MeOH	777	223,000	807	30	10.5	23415	–	–	–
	DMF	788	188,000	818	30	13.7	25756	–	–	–
	DMSO	776	210,000	810	34	13.0	27300	–	–	–
CyD7	CH_2Cl_2	857	678,000	912	55	1.3	8817	0.17	0.08	5.81
	MeOH	844	594,000	905	61	0.9	5346	–	–	–
	DMF	854	389,000	920	66	1.0	3888	–	–	–
	DMSO	841	459,000	905	64	1.1	5049	–	–	–
CyD7.5	CH_2Cl_2	873	648,000	927	54	1.4	9075	0.24	0.06	4.11
	MeOH	861	513,000	920	59	1.0	5134	–	–	–
	DMF	872	332,000	940	68	1.2	3979	–	–	–
	DMSO	861	524,000	927	66	0.7	3669	–	–	–
CyD7Et	CH_2Cl_2	861	701,000	915	54	1.3	9116	0.19	0.07	5.19
	MeOH	856	616,000	915	59	1.0	6162	–	–	–
	DMF	864	428,000	926	62	1.0	4282	–	–	–
	DMSO	854	584,000	921	67	0.8	4675	–	–	–
CyD7Bn	CH_2Cl_2	877	679,000	931	54	1.7	11540	0.17	0.1	5.78
	MeOH	867	565,000	928	61	1.3	7348	–	–	–
	DMF	878	387,000	941	63	1.3	5036	–	–	–
	DMSO	868	529,000	933	65	1.2	6350	–	–	–

[a]Relative fluorescence quantum yield: Φ_F of dimers were determined using **ECY** as a reference (in $CHCl_3$, Φ_F = 19%); Φ_F of monomer was determined using **ICG** as a reference (in MeOH, Φ_F = 7.8%); [b]brightness = ε × Φ_F.

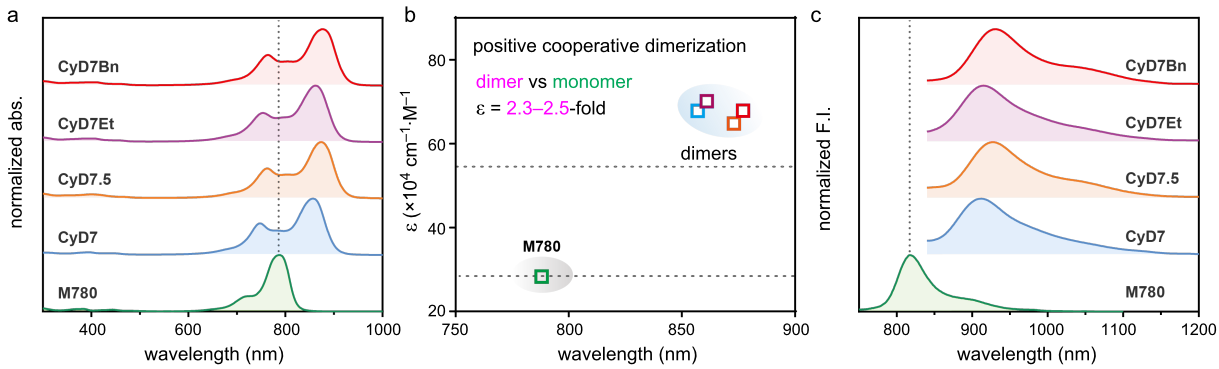

Figure 3: Comparison of absorption wavelength (a), molar absorptivity (b), and emission wavelength (c) of monomer and dimers.

To evaluate the in vivo biodistribution of **CyD7Bn** NPs, the mice were sacrificed 24 h post-injection, and the major metabolic organs were immediately dissected for ex vivo fluorescence imaging (Figure 4i and 4j). The fluorescence signals predominantly accumulated in the liver, spleen, and kidneys, indicating that **CyD7Bn** NPs were cleared through multiple organ pathways. This biodistribution profile was favorable for minimizing nonspecific accumulation and enhancing the in vivo safety of the nanoprobes.

In vivo NIR fluorescence imaging of lymph vessels and lymph nodes

Near-infrared lymphatic fluorescence imaging plays a critical role in assessing lymphatic drainage function, preventing

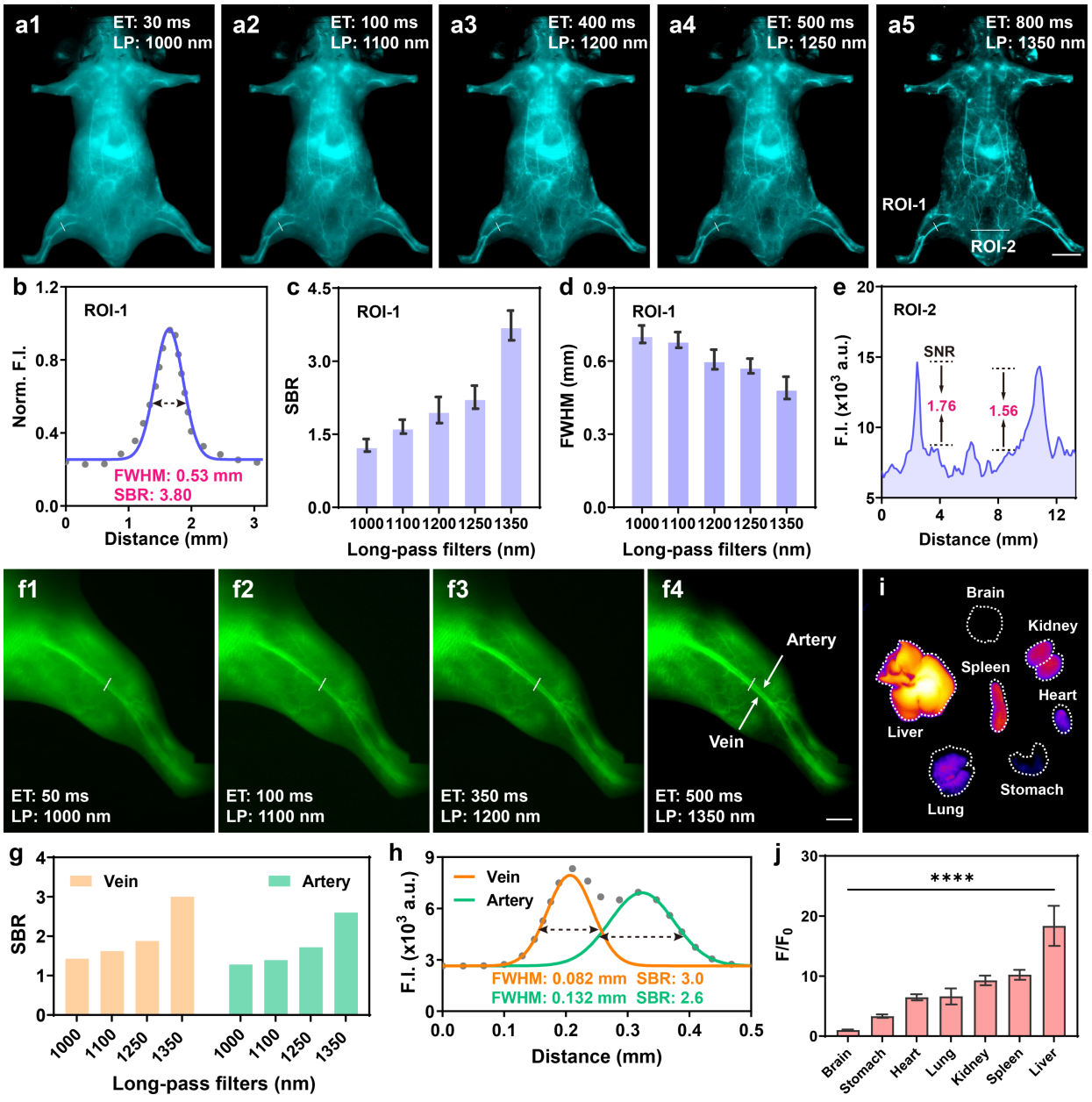

Figure 4: a1–a5) NIR fluorescence imaging of systemic vasculature in BALB/c mice with various long-pass filters after intravenous injection of **CyD7Bn** NPs (100 µL, 1 mg/kg) via the tail vein. Imaging conditions: 880 nm laser excitation, 100 mW·cm^{-2} power density, 1000–1350 nm long-pass filter. Scale bar: 10 mm. b–e) Comparison of SBR, FWHM, and SNR in ROI-1 or ROI-2. f1–f4) NIR fluorescence imaging of vascular structures in the hindlimb of BALB/c mice with different long-pass filters. Arrows indicate the femoral artery and femoral vein, respectively. Imaging conditions: 880 nm laser excitation, 30 mW·cm^{-2} power density, 1000–1350 nm long-pass filter. Scale bar: 2 mm. g, h) Comparison of SBR and FWHM for the femoral artery and femoral vein within the hindlimb. i) Ex vivo fluorescence imaging of major organs 24 h post-injection of **CyD7Bn** NPs. j) Comparison of relative fluorescence intensity.

lymphatic-related diseases, and exploring the pathogenesis of various immune disorders. In cases of lymphatic malformations, lymphangitis, and lymphatic tumors, surgical resection and drainage guided by lymphatic imaging are required [20-24]. To this end, we further investigated whether **CyD7Bn** NPs possess high resolution and high sensitivity for in vivo imaging of lymphatic vessels and lymph nodes. **CyD7Bn** NPs (20 µL, 0.2 mg/kg) were locally injected into the hindlimb footpad, gluteal muscle, and forelimb footpad of mice, and the lymphatic vessels and lymph nodes in different regions were imaged (Figure 5a, 5d, and 5g).

The FDA-approved **ICG** maintained fluorescence brightness for only 10 min during lymphatic imaging, with low image resolu-

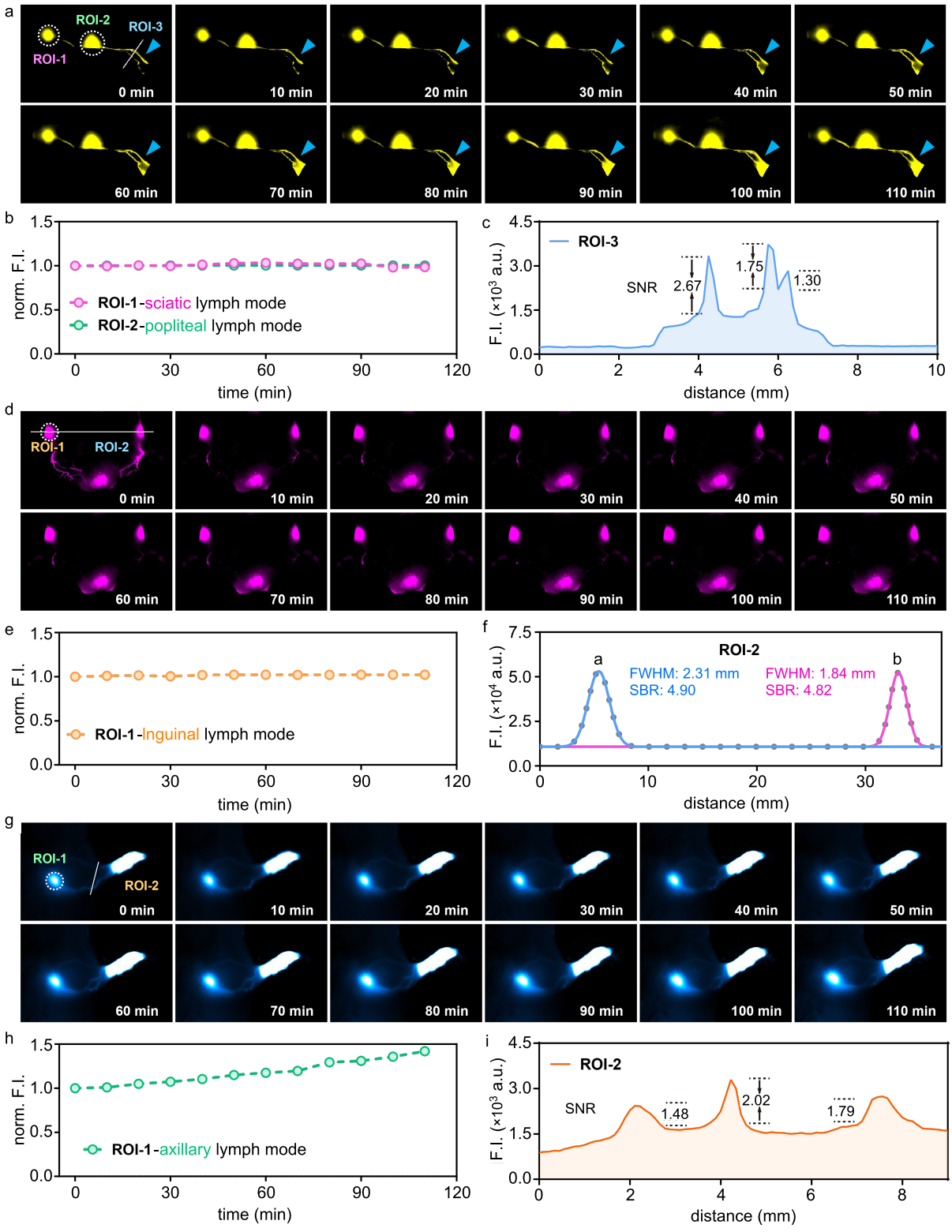

Figure 5: a), d) and g) NIR fluorescence imaging of lymphatic vessels and lymph nodes at different time points after injection of **CyD7Bn** NPs (20 μL, 0.2 mg/kg) via the hindlimb footpad, gluteal muscle, and forelimb footpad, respectively. Imaging conditions: 880 nm laser excitation, 30 mW·cm^{-2} power density, 1250 nm long-pass filter. b), e) and h) Time-dependent fluorescence intensity changes in the sciatic, popliteal, inguinal, and axillary lymph nodes, respectively. c), f) and i) SBR, FWHM, and SNR comparison of the ROI-1, ROI-2, or ROI-3.

tion, blurred morphology, strong tissue autofluorescence, and scattering interference [25-27]. Remarkably, **CyD7Bn** NPs rapidly highlighted the lymph nodes via the lymphatic vessels, and the fluorescence brightness in the sciatic, popliteal, inguinal, and axillary lymph nodes remained essentially unchanged for up to 110 min (Figure 5b, 5e, and 5h). The diameters of the inguinal lymphatic vessels were analyzed by Gaussian fitting, yielding values of 2.32 mm and 1.84 mm, respectively, with SBR values consistently above 4.8 (Figure 5c, 5f, and 5i). These results demonstrate the potential of **CyD7Bn** NPs for long-term lymphatic visualization and image-guided surgical navigation.

Conclusion

In summary, single-bond-tethered dimerization converts the molar absorptivity of cyanine dyes from an intrinsic "natural gift" into an engineerable parameter. The dimers **CyD7**, **CyD7.5**, **CyD7Et**, and **CyD7Bn**, in which two cyanine chromophores are linked by a single bond, feature well-aligned transition dipole moments and strong intramolecular exciton coupling, while interchromophore π-conjugation remains limited, as evidenced by absorption maxima red-shifted by only 69–88 nm. All dimers exhibit positive cooperative light harvesting, with molar absorptivities of 648,000–701,000 $M^{-1}\cdot cm^{-1}$ in CH_2Cl_2, 2.3–2.5-fold that of monomer **M780**. Although fluorescence quantum yields and lifetimes decrease owing to enhanced non-radiative decay, **CyD7Bn** retains a brightness above 10,000 $M^{-1}\cdot cm^{-1}$. Its nanoparticles enable high-contrast whole-body vascular imaging, submillimeter discrimination of the femoral artery and vein, and lymphatic visualization for up to 110 min.

These results establish single-bond-tethered dimerization as a broadly applicable strategy for constructing NIR photofunctional materials with ultrahigh molar absorptivity. Similarly, this structure–property relationship may be applicable to alternative fluorochromic scaffolds, e.g., xanthene, BODIPY, squareine, and relyene. Besides, another important question to address is how to further improve the fluorescence quantum yields of such single-bond-tethered dye dimers.

Supporting Information

Supporting Information File 1

UV–vis absorption and fluorescence emission spectra; fluorescence lifetime spectra; $^{1}H/^{13}C$ NMR, and HRMS spectra.
[https://www.beilstein-journals.org/bjoc/content/supplementary/1860-5397-22-146-S1.pdf]

Funding

This work was supported by the National Key Research and Development Program of China (Nos. 2022YFD1700800), and the National Natural Science Foundation of China (Nos. 22278138).

Author Contributions

Bingya Wang: investigation; writing – original draft; writing – review & editing. Qin Yan: investigation. Bei Zhao: investigation. Guangbo Ge: project administration; writing – review & editing. Xuhong Qian: conceptualization; supervision; writing – review & editing. Xiao Luo: conceptualization; resources; supervision; writing – review & editing. Youjun Yang: conceptualization; funding acquisition; project administration; resources; writing – original draft; writing – review & editing.

ORCID® iDs

Qin Yan - https://orcid.org/0009-0002-6488-4899
Youjun Yang - https://orcid.org/0000-0001-7085-6048

Data Availability Statement

Data generated and analyzed during this study is available from the corresponding author upon reasonable request.

References

1. Tan, W.; Wang, X.; Wen, D.; Yu, Y.; Ma, Y. *Chem. Soc. Rev.* **2026,** *55,* 9391–9414. doi:10.1039/d6cs00570e
2. Yang, M.; Ou, X.; Zhang, J.; Sun, J.; Kwok, R. T. K.; Lam, J. W. Y.; Fan, J.; Tang, B. Z. *Adv. Funct. Mater.* **2025,** *35,* 2411838. doi:10.1002/adfm.202411838
3. Yang, Y.; Sun, C.; Wang, S.; Yan, K.; Zhao, M.; Wu, B.; Zhang, F. *Angew. Chem., Int. Ed.* **2022,** *61,* e202117436. doi:10.1002/anie.202117436
4. Zhang, Y.; Wang, B.; Yan, Q.; Lu, X.; Zhang, X.; Yao, C.; Qi, Y.; Yang, M.; Ge, G.; Qian, X.; Luo, X.; Yang, Y. *J. Am. Chem. Soc.* **2025,** *147,* 40739–40750. doi:10.1021/jacs.5c13660
5. Shi, Y.; Yang, W.; Zhang, H.; Zhong, C.; Gong, S.; Yang, C. *Adv. Funct. Mater.* **2025,** *35,* 2423408. doi:10.1002/adfm.202423408
6. Zhao, Y.; Zhang, R.-R.; Wang, N.; Tian, X.-L.; Zhang, L.-N.; Xia, W.-L.; Wang, Z.-Y.; Yu, X.-Q.; Li, K. *Mater. Horiz.* **2025,** *12,* 10698–10708. doi:10.1039/d5mh01254f
7. Gu, H.; Yuan, P.; Zhang, J.; Xia, X.; Pan, Q.; Liu, W.; Zhao, X.; Sun, W.; Du, J.; Fan, J.; Peng, X. *J. Am. Chem. Soc.* **2025,** *147,* 20778–20789. doi:10.1021/jacs.5c04044
8. Huang, H.; Ma, D.; Liu, Q.; Huang, D.; Zhao, X.; Yao, Q.; Xiong, T.; Long, S.; Du, J.; Fan, J.; Peng, X. *CCS Chem.* **2022,** *4,* 3627–3636. doi:10.31635/ccschem.021.202101479
9. Gu, H.; Zhang, J.; Yuan, P.; Zheng, Z.; Liu, W.; Xia, X.; Sun, W.; Du, J.; Fan, J.; Peng, X. *Chin. Chem. Lett.* **2026,** *37,* 111119. doi:10.1016/j.cclet.2025.111119
10. Huang, H.; Liu, Q.; Zhu, J.-H.; Tong, Y.; Huang, D.; Zhou, D.; Long, S.; Wang, L.; Li, M.; Chen, X.; Peng, X. *Aggregate* **2025,** *6,* e706. doi:10.1002/agt2.706
11. Yu, J.-F.; Li, J.; Li, M. *ACS Sens.* **2024,** *9,* 3581–3593. doi:10.1021/acssensors.4c00561

12. Ma, Y.; Han, M.; Zhu, H.; Cui, F.; Qiao, Y.; Yin, Y.; Zhao, X.; Xi, R.; Meng, M. *Anal. Chem. (Washington, DC, U. S.)* **2025,** *97,* 12338–12346. doi:10.1021/acs.analchem.5c01434
13. Pan, Y.; Lei, S.; Liu, Q.; Chen, K.; Zhang, Y.; Li, M.; Liu, Y.; Bai, M.; Guo, H.; Huang, P.; Lin, J. *Cell Rep. Phys. Sci.* **2026,** *7,* 103027. doi:10.1016/j.xcrp.2025.103027
14. Wang, X.; Zhou, J.; Wang, M.; Wang, Y.; Shen, Z.; Sun, H.; Hu, Z.; Luo, X.; Yang, Y.; Chen, J. *Angew. Chem., Int. Ed.* **2025,** *64,* e202425422. doi:10.1002/anie.202425422
15. Liu, Y.; Li, Y.; Koo, S.; Sun, Y.; Liu, Y.; Liu, X.; Pan, Y.; Zhang, Z.; Du, M.; Lu, S.; Qiao, X.; Gao, J.; Wang, X.; Deng, Z.; Meng, X.; Xiao, Y.; Kim, J. S.; Hong, X. *Chem. Rev.* **2022,** *122,* 209–268. doi:10.1021/acs.chemrev.1c00553
16. Kim, K.; Lee, J.-U.; Nam, D.; Cheong, H. *ACS Nano* **2016,** *10,* 8113–8120. doi:10.1021/acsnano.6b04471
17. Ma, J.; Luo, F.; Hsiung, C.-H.; Dai, J.; Tan, Z.; Ye, S.; Ding, L.; Shen, B.; Zhang, X. *Angew. Chem., Int. Ed.* **2024,** *63,* e202403029. doi:10.1002/anie.202403029
18. Zhu, Y.; Wu, P.; Liu, S.; Yang, J.; Wu, F.; Cao, W.; Yang, Y.; Zheng, B.; Xiong, H. *Angew. Chem., Int. Ed.* **2023,** *62,* e202313166. doi:10.1002/anie.202313166
19. Wang, Y.; Zhou, D.; Ma, H.; Liu, D.; Liang, Y.; Zhu, S. *Eur. J. Nucl. Med. Mol. Imaging* **2024,** *51,* 2941–2952. doi:10.1007/s00259-024-06702-0
20. Kosaka, N.; Ogawa, M.; Sato, N.; Choyke, P. L.; Kobayashi, H. *J. Invest. Dermatol.* **2009,** *129,* 2818–2822. doi:10.1038/jid.2009.161
21. Nakajima, Y.; Asano, K.; Mukai, K.; Urai, T.; Okuwa, M.; Sugama, J.; Nakatani, T. *Sci. Rep.* **2018,** *8,* 7078. doi:10.1038/s41598-018-25383-y
22. Pang, Z.; Yan, W.; Yang, J.; Li, Q.; Guo, Y.; Zhou, D.; Jiang, X. *ACS Nano* **2022,** *16,* 16019–16037. doi:10.1021/acsnano.2c03752
23. Li, M.; Sun, B.; Zheng, X.; Ma, S.; Zhu, S.; Zhang, S.; Wang, X. *ACS Sens.* **2024,** *9,* 1339–1348. doi:10.1021/acssensors.3c02322
24. Guo, J.; Zhu, Y.; Qu, Y.; Zhang, L.; Fang, M.; Xu, Z.; Wang, T.; Qin, Y.; Xu, Y.; Li, Y.; Chen, Y.; Fu, H.; Liu, X.; Liu, Y.; Liu, C.; Gao, Y.; Cui, M.; Zhou, K. *J. Med. Chem.* **2024,** *67,* 16820–16834. doi:10.1021/acs.jmedchem.4c01662
25. Han, T.; Wang, Y.; Xu, J.; Zhu, N.; Bai, L.; Liu, X.; Sun, B.; Yu, C.; Meng, Q.; Wang, J.; Su, Q.; Cai, Q.; Hettie, K. S.; Zhang, Y.; Zhu, S.; Yang, B. *Chem. Sci.* **2022,** *13,* 13201–13211. doi:10.1039/d2sc05651h
26. Qi, S.; Wang, Y.; Zhu, Y.; Zhang, X.; Wang, X.; Yu, X.; Yang, K.; Bai, B.; Feng, Y.; Lei, J.; Zhang, K.; Lu, Z.; Zhu, S.; Du, J.; Yu, G. *Nano Today* **2023,** *49,* 101795. doi:10.1016/j.nantod.2023.101795
27. Zhang, X.-X.; Yang, F.; Zhao, X.; Wu, Q.; He, L.; Li, Z.; Zhou, Z.; Ren, T.-B.; Zhang, X.-B.; Yuan, L. *Angew. Chem., Int. Ed.* **2024,** *63,* e202410666. doi:10.1002/anie.202410666

License and Terms

This is an open access article licensed under the terms of the Beilstein-Institut Open Access License Agreement (https://www.beilstein-journals.org/bjoc/terms), which is identical to the Creative Commons Attribution 4.0 International License (https://creativecommons.org/licenses/by/4.0). The reuse of material under this license requires that the author(s), source and license are credited. Third-party material in this article could be subject to other licenses (typically indicated in the credit line), and in this case, users are required to obtain permission from the license holder to reuse the material.

The definitive version of this article is the electronic one which can be found at:
https://doi.org/10.3762/bjoc.22.146